



OPEN

SUBJECT AREAS:

MECHANICAL
PROPERTIES

METALS AND ALLOYS

Bulk metallic glass composite with good tensile ductility, high strength and large elastic strain limit

Fu-Fa Wu^{1,2}, K. C. Chan¹, Song-Shan Jiang², Shun-Hua Chen¹ & Gang Wang³

Received

18 March 2014

Accepted

21 May 2014

Published

16 June 2014

Correspondence and requests for materials should be addressed to K.C.C. (mfkchan@inet.polyu.edu.hk)

¹Advanced Manufacturing Technology Research Centre, Department of Industrial and Systems Engineering, The Hong Kong Polytechnic University, Kowloon, Hong Kong, China, ²School of Materials Science and Engineering, Liaoning University of Technology, Jinzhou 121001, China, ³Laboratory for Microstructures, Shanghai University, Shanghai 200444, China.

Bulk metallic glasses exhibit high strength and large elastic strain limit but have no tensile ductility. However, bulk metallic glass composites reinforced by in-situ dendrites possess significantly improved toughness but at the expense of high strength and large elastic strain limit. Here, we report a bulk metallic glass composite with strong strain-hardening capability and large elastic strain limit. It was found that, by plastic predeformation, the bulk metallic glass composite can exhibit both a large elastic strain limit and high strength under tension. These unique elastic mechanical properties are attributed to the reversible B2↔B19' phase transformation and the plastic-predeformation-induced complicated stress state in the metallic glass matrix and the second phase. These findings are significant for the design and application of bulk metallic glass composites with excellent mechanical properties.

The elastic strain limit, along with the elastic limit (the highest stress at which permanent deformation will not occur), is an important factor for engineering materials¹. By eliminating the extrinsic flaws and decreasing the internal structural defects, submicro-sized metallic glasses (MGs) can reach an outstandingly large elastic strain limit of more than 3%²⁻⁵. The elastic strain limit for bulk metallic glasses (BMGs) is almost 2%, which is also significantly high in contrast with common engineering materials, though smaller than nanosized MGs. However, BMGs usually fail catastrophically by the fast propagation of a major shear band, leaving zero global plastic strain under tension⁶⁻⁸. Therefore, second phases are in-situ or ex-situ introduced to reinforce the MG matrices⁹⁻¹³, such as dendrite-reinforced Zr- or Ti-based bulk metallic glass composites (BMGCs)¹⁴⁻¹⁸.

Though their toughness or ductility is significantly increased, the yield strength and the elastic strain limit of BMGCs are decreased dramatically in contrast to monolithic BMGs^{15,18,19}. Usually, the second phases have a relatively small elastic strain limit (not larger than 1%), which results in the premature yield of the BMGCs. Furthermore, the volume fraction of the soft second phase should be higher than 50% to toughen the MG matrix, which severely decreases the elastic strain limit and the strength of BMGCs¹⁴⁻¹⁸. Therefore, a suitable second phase is the key factor for improving the strength, elastic strain limit and ductility of BMGCs. To conserve the large strain limit of BMGs, the second phases also should have a large strain limit not less than 2%. Further, to keep the high strength of BMGs, the second phases should originally have a high enough strength or the soft second phases can be strengthened to a higher strength. It is noted that, in NiTi shape memory alloys, the metastable B2 phase can be strain hardened from less than 100 MPa to more than 1200 MPa, and can undergo a reversible phase transformation of bcc B2↔monoclinic B19', which endows the alloy with high yield strength and superelasticity²⁰. Therefore, by adding a metastable B2 phase and suitable plastic predeformation, the B2 reinforced BMGCs²¹⁻²⁹ should exhibit a good match in elasticity, strength, and ductility. For example, CuZr-based BMGC with nanosized B2 phase exhibited tensile ductility³⁰, and NiTi-based BMGC also showed a good combination of high strength and large pseudo-elasticity under compression^{31,32}.

In this work, we report a metastable B2 reinforced BMGC (B2-BMGC) with excellent plastic deformation capability under tension. We demonstrate that the B2 phase effectively improves the plastic deformation capability of the B2-BMGC under tension, and the plastic predeformation endows this B2-BMGC with high strength and a large elastic strain limit by reversible B2↔B19' phase transformation.

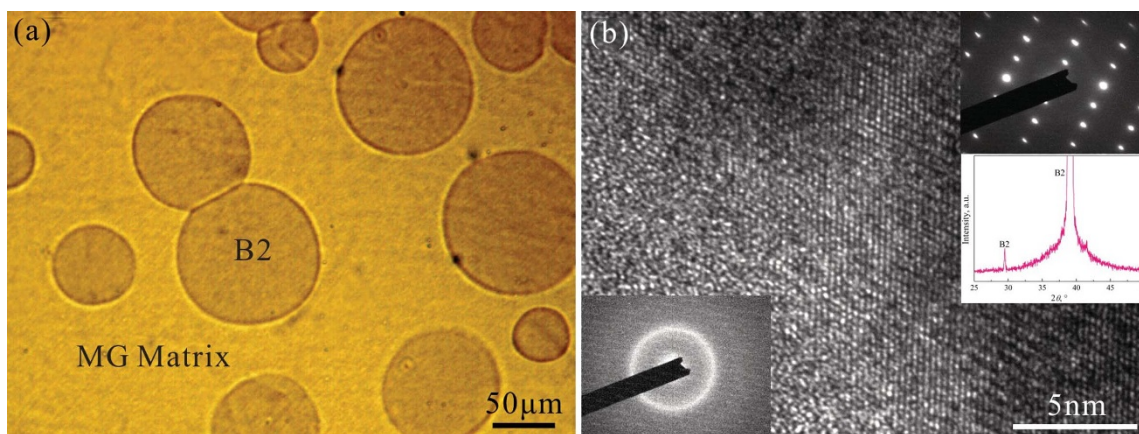


Figure 1 | (a) OM metallograph showing the microstructure of the as-cast B2-BMGC. The round particles are the B2 phase, and the matrix is amorphous MG. (b) HRTEM image of the interface between the B2 phase and the amorphous matrix. Inset at the lower left corner shows the selected area diffraction pattern of the amorphous structure; the inset at the upper right corner shows the selected area diffraction pattern of the crystalline structure, and the inset at the middle right shows the X-ray diffraction pattern of the B2-BMGC.

Results

Microstructure of as-cast B2-BMGC. Figure 1a shows an optical metallograph of the microstructure of the as-cast B2-BMGC. The round and dark particles are B2 crystals, which are homogeneously distributed in the amorphous MG matrix. The average chemical compositions for the B2 phase and the amorphous MG matrix are detected by energy-dispersive spectroscopy (EDS) to be $Zr_{52.1}Cu_{41.7}Al_{3.9}Nb_{2.3}$ and $Zr_{50.7}Cu_{42.2}Al_{4.1}Nb_{3.0}$, respectively. It is clear that the difference between the chemical compositions of the B2 phase and the amorphous MG matrix is very small, which

indicates the precipitation of B2 phase from the melt during solidification does not involve strong element diffusion, like that usually occurring in in-situ dendrite-reinforced BMGCs¹⁴. The volume fraction of the B2 phase is about 32.2% and the average grain size of the B2 particles is $67 \pm 5 \mu\text{m}$ in diameter. Figure 1b shows the high-resolution transmission electron microscope (HRTEM) image of the interface between the B2 phase and the amorphous MG matrix. The electron diffraction patterns show that the disorder region is fully amorphous (see lower left inset in Fig. 1b) and the adjacent region is of long-range order (see upper

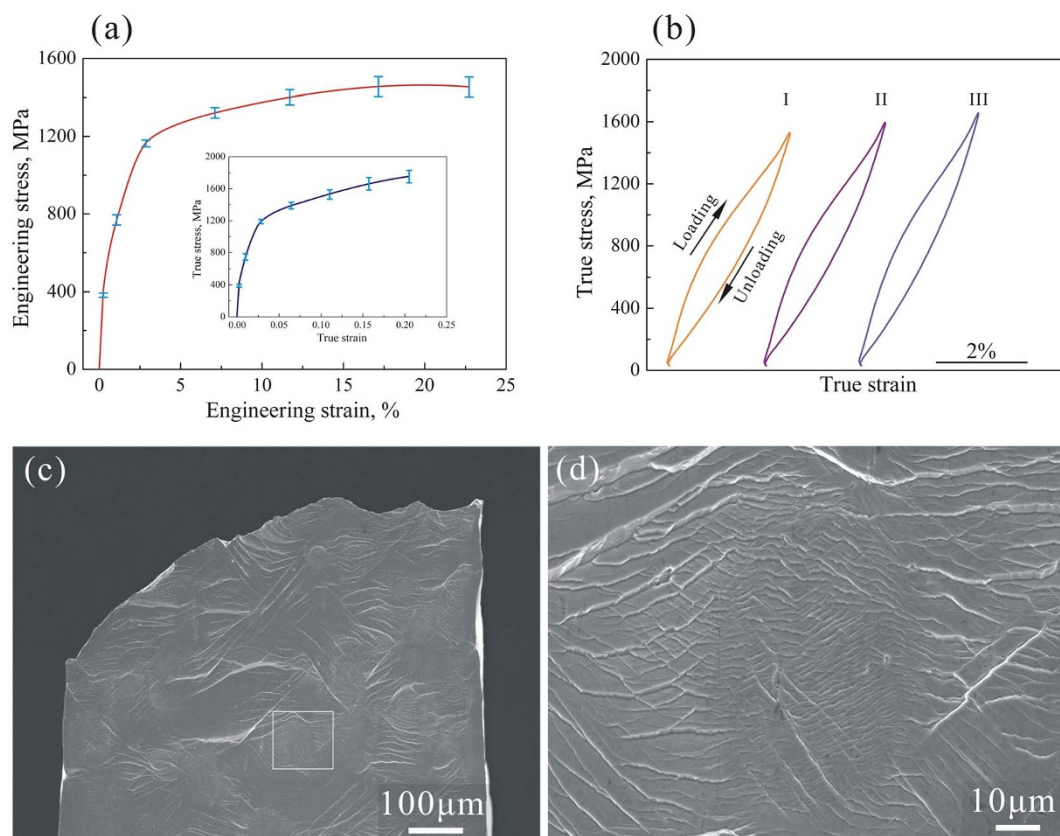


Figure 2 | (a) Engineering tensile stress-strain curve of the as-cast B2-BMGC showing large homogeneous plastic deformation capability. The inset in (a) is the true stress-strain curve of the as-cast B2-BMGC showing significant strain-hardening. The error bars were based on standard deviation. (b) cyclic loading stress-strain curves showing large elastic strain limit and nonlinear elasticity for the (I) 10.2%, (II) 12.6%, and (III) 15.0% plastically predeformed B2-BMGCs. (c) and (d) Deformation feature of the as-cast B2-BMGC after tensile fracture.

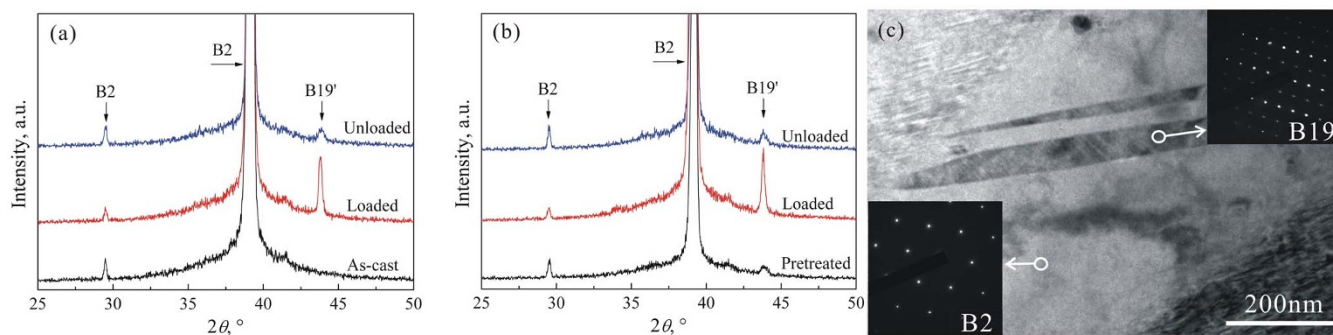


Figure 3 | XRD patterns showing the phase transformation during (a) plastic predeformation and (b) elastic reloading. During plastic predeformation, a sharp transformation of B2→B19' is detected, and a residual B19' is also detected after plastic predeformation, as shown in (a). During the elastic reloading of the plastically predeformed B2-BMGC, the B19' peak is strengthened, indicating that more B2 is transformed to B19', and a reversible transformation of B19'→B2 is observed, as shown in (b). (c) TEM image showing the B19' phase transformed from B2 phase in the plastically predeformed B2-BMGC.

right inset in Fig. 1b). The crystalline phase is further confirmed to be B2 phase with a body-centered cubic structure by the use of X-ray diffraction (see middle right inset in Fig. 1b).

Tensile deformation of as-cast B2-BMGC. Figure 2a shows the engineering stress-strain curve of the as-cast B2-reinforced BMGC subjected to tensile loading. It is seen that the sample underwent a large homogeneous plastic deformation with a total engineering strain of 22.3% on average (the maximum engineering plastic strain before fracture was 19.3%). Close examination indicates that the stress-strain curve can be divided into four stages. Firstly, the sample undergoes an initial linear elastic stage under relatively low stress. In this region, both the B2 phase and the MG matrix synchronously deform elastically. Secondly, the sample slightly yields at 387 MPa with recoverable elastic strain of about 0.2%. In this region, the MG matrix is still in elastic state, but the B2 phase reaches its yield point and begins to plastically deform. Thirdly, the sample yields apparently at a stress of 1100 MPa and is strain-hardened to more than 1400 MPa at an engineering strain of 17.8%. Fourthly, a small stress decrease starts and is a prelude to the beginning of tensile instability and final fracture. The inset in Fig. 2a is the true stress-strain curve corresponding to the engineering curve for the as-cast B2-BMGC. It demonstrates that the as-cast B2-BMGC possesses a strong strain-hardening capability under tension: beginning from the apparent yield stress of $\sigma_s = 1100$ MPa, the true stress continues increasing to the fracture strength of 1765 MPa, as seen in the inset of Fig. 2a. The average strain-hardening rate ($\theta = \frac{d\sigma}{d\varepsilon}$) in the smooth region (true strain between 0.05 and 0.15) is 3366 MPa, and the normalized strain-hardening rate ($\theta_0 = \theta/\sigma_s$) is 3.1, which is higher than most previously reported BMGCs²⁸.

Elastic response of plastically predeformed B2-BMGC. Figure 2b shows the true tensile stress-strain curves of the B2-BMGC after plastic predeformation with a total engineering tensile strain of 10.2%, 12.6%, and 15.0%, as marked with cycles I, II, and III, respectively. It indicates that the B2-BMGC exhibits nonlinear elastic stress-strain behavior, which is significantly different from the linear elasticity of typical monolithic BMGs and other BMGCs⁶. The elastic strain limit is about 2.7%, which is remarkably larger than that (about 2%) of monolithic BMGs or that (usually small than 2%) of other reported BMGCs, and far larger than that (0.2%) of the as-cast B2-BMGC. Further examination reveals that the nonlinear elastic stress-strain curves can be divided into three segments: an initial linear segment, a following parabolic segment, and a final steep segment. The first linear segment is attributed to the synchronized linear elastic response of both the MG matrix and

the B2 phase at relatively low stress. The second parabolic segment demonstrates obvious nonlinear elastic stress-strain behavior and a continuously reducing slope, which is mainly triggered by the B2→B19' phase transformation at relatively high stress level. The third steep segment reflects that the B2→B19' phase transformation has reached the saturation. During this segment, the transformed B19', the residual B2, and the MG matrix all elastically deform synchronously.

Structural evolution of B2-BMGC during plastic predeformation and elastically reloading. Figure 3a shows the X-ray diffraction (XRD) patterns of the B2-BMGC during plastic predeformation. For the as-cast B2-BMGC, it shows that a strong diffraction peak ($2\theta = 39.1^\circ$) of the B2 phase superimposed in the scattering diffraction peak of the amorphous MG matrix, as seen in Fig. 3a. When plastically predeformed with a total engineering tensile strain of 10.2%, a sharp diffraction peak appears at $2\theta = 43.8^\circ$, which is confirmed to be the B2→B19' phase transformation. After removing the load, the diffraction peak at $2\theta = 43.8^\circ$ decreased in intensity, but still existed, implying that the B19' remained although some B19' transformed backwards to B2, as shown in Fig. 3a and 3c. Figure 3b shows the XRD patterns of the plastically predeformed B2-BMGC during elastically reloading. It shows that, with the load increasing, the diffraction peak at $2\theta = 43.8^\circ$ was strengthened, which means more of the B2 phase was transformed to the B19' phase. Once the load decreased, the diffraction peak of the B19' phase weakened again, as in its original profile (Fig. 3b). This structural evolution revealed by XRD is consistent with the nonlinear elastic stress-strain behavior of the plastically predeformed B2-BMGC (see Fig. 2b).

Discussion

Large plastic stability of as-cast B2-BMGC under tension. The above results indicate that the as-cast B2-BMGC can undergo large tensile plastic deformation. The plastic strain before fracture is about 19.3%, and the normalized strain-hardening rate ($\theta_0 = \theta/\sigma_s$) is about 3.1. The prominent tensile plastic deformation capability of the as-cast B2-BMGC can be attributed to the high strain-hardening capability of the B2 phase and its effectiveness in activating multiple shear bands in the MG matrix. It was previously reported that the normalized strain-hardening rate of CuZr-based B2 phase was about 17.4, which is far larger than that of β dendrite in-situ formed in Ti- or Zr-based BMGCs²⁸. For instance, the normalized strain-hardening rate of the β dendrite $Zr_{71}Ti_{16.3}Nb_{10}Cu_{1.8}Ni_{0.9}$ is 1.7, which is only one tenth of the present B2 phase²⁸. From the viewpoint of the microstructure, the B2→B19' phase transformation can produce hierarchical deformation structures with macro-twin, micro-twin, stacking fault and dislocation^{33,34}, which yields dense

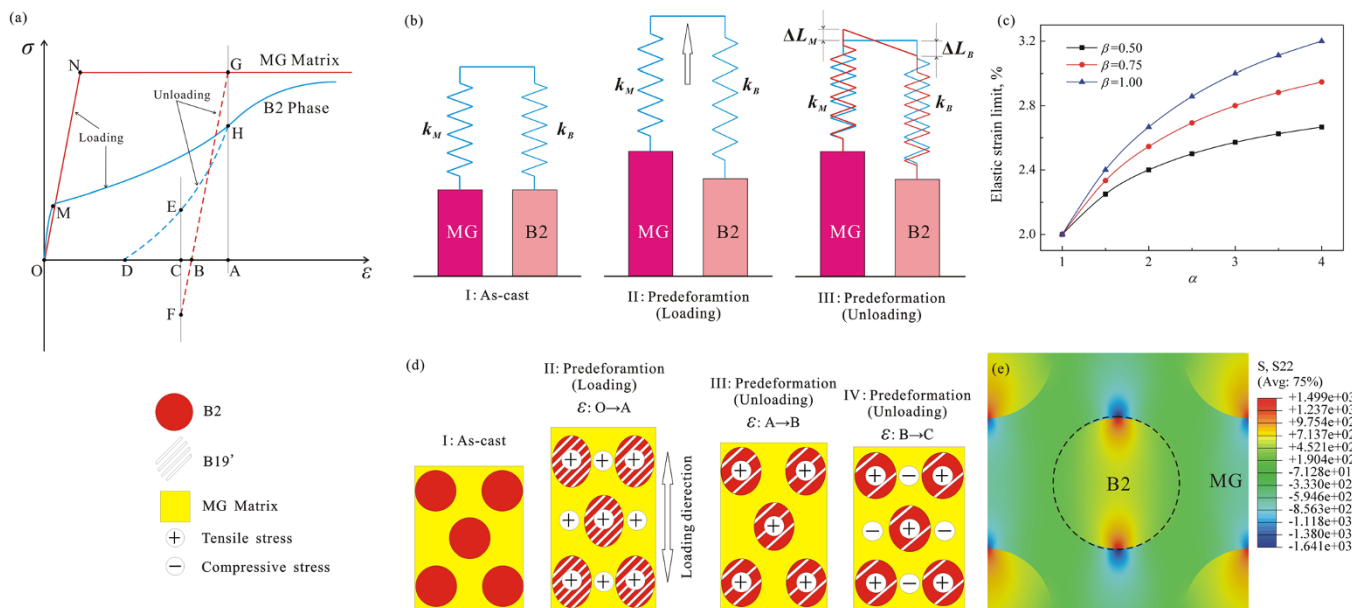


Figure 4 | (a) Schematic illustration of the loading history for the B2-BMGC during plastic predeformation and elastic reloading. (b) Model of parallel connection of two rigid-plastic bodies series-connected with ideal-elastic bodies for the B2-BMGC during plastically predeformation. (c) The elastic strain limit of the B2-BMGC related to α and β . (d) Schematic illustration of stress-strain status of B2 phase and MG matrix in the B2-BMGC during plastic predeformation. (e) FEM simulation result showing the stress state of the plastically predeformed B2-BMGC.

stress-concentration sites at the interface and can trigger profuse tiny multiple shear bands in the MG matrix^{24,29,35}. Even shear bands excited from one B2 crystal can have different propagation directions and can intersect with each other, as shown in Fig. 2d. Furthermore, these shear bands will propagate forwards and intersect with those excited from the neighbouring B2/MG interfaces. Therefore, the B2 phase is a very effective exciter for the initiation of multiple shear bands in the MG matrix. However, small β dendrites can only excite a few shear bands and can easily cut off by the propagating shear bands. The shear bands around one dendrite almost have the same propagation direction, and their interaction among them is very limited^{28,36,37}.

Large elastic strain limit of plastically predeformed B2-BMGC.

Usually, the elastic strain limit of monolithic BMGs is about 2.0%^{38,39}, while the elastic strain limit of classical BMGCs is much smaller than 2.0%¹⁷. However, the present plastically predeformed B2-BMGC has a large elastic strain limit of 2.7%. This unique deformation behavior of the B2-BMGC can be explained as follows. Figure 4a schematically shows the loading history of the B2-BMGC during plastically predeformation: lines ON, NG, and GB are the stress-strain curves for the elastic deformation, plastic deformation, and elastic recovery of the MG matrix; lines OM, MH, HD are the stress-strain curves for the elastic deformation, plastic deformation, and elastic recovery of the B2 phase; point C is the final stress balance point after unloading. Both the MG matrix and the B2 phase can be regarded as a parallel connection of two rigid-plastic bodies series-connected with ideal-elastic bodies, as shown in Fig. 4b-I. For the as-cast B2-BMGC, it is assumed that the MG matrix and the B2 phase have the same length. When plastically predeformed to a certain strain, due to the B2 \leftrightarrow B19' reverse phase transformation, the B2 phase has a larger elastic strain limit than the MG matrix, while the MG matrix has a larger plastic strain than the B2 phase, though they have the same total strain, i.e.

$$\varepsilon_e^M + \varepsilon_p^M = \varepsilon_e^B + \varepsilon_p^B. \quad (1)$$

Here ε_e^M is the elastic strain limit of the MG matrix, ε_p^M the plastic strain of the MG matrix, ε_e^B the elastic strain limit of the B2

phase, and ε_p^B the plastic strain of the B2 phase, as shown in Fig. 4b-II. After plastic predeformation, the external force is removed, and the elastic strain will tend to recover. In an ideal free-standing situation, both MG matrix and B2 phase will recover to the zero stress state, as shown in the red spring in Fig. 4b-III. However, due to the elastic strain mismatch and the mutual constraint, the recovery of the B2 phase will be inhibited by the MG matrix, while the recovery of the MG matrix will be promoted by the recovery of the B2 phase. Therefore, the MG matrix will be in a compressive stress state and the B2 phase will be in a tensile stress state, as shown in the blue spring in Fig. 4b-III. Thus, we have

$$\varepsilon_e^{M'} + \varepsilon_p^M = \varepsilon_e^{B'} + \varepsilon_p^B. \quad (2)$$

Here $\varepsilon_e^{M'}$ and $\varepsilon_e^{B'}$ are the residual elastic strains in the MG matrix and the B2 phase, respectively. According to the static balance between the MG matrix and the B2 phase, one gets

$$E_M \varepsilon_e^{M'} + E_B \varepsilon_e^{B'} = 0. \quad (3)$$

E_M and E_B are the elastic modulus of the MG matrix and the B2 phase after plastic predeformation. Substituting Equations (1) and (2) to Equation (3), we get the residual elastic strain in the MG matrix as

$$\varepsilon_e^{M'} = -\frac{E_B(\varepsilon_e^B - \varepsilon_e^M)}{E_M + E_B}, \quad (4)$$

and the residual elastic strain in the B2 phase is

$$\varepsilon_e^{B'} = \frac{E_M(\varepsilon_e^B - \varepsilon_e^M)}{E_M + E_B}. \quad (5)$$

Obviously, Equations (4) and (5) demonstrate that the residual elastic strain in the MG matrix is compressive, while the residual elastic strain in the B2 phase is tensile. Due to the elastic strain limit of the MG matrix being smaller than that of B2 phase, the elastic strain limit of the B2-BMGC will be decided by the MG matrix. Therefore, when subject to tensile loading, the apparent elastic strain limit of the plastically predeformed B2-BMGC is



$$\varepsilon_e = \varepsilon_e^M - \varepsilon_e^{M'} = \varepsilon_e^M + \frac{E_B(\varepsilon_e^B - \varepsilon_e^M)}{E_M + E_B}. \quad (6)$$

Substituting $E_M = \sigma_e^M / \varepsilon_e^M$ and $E_B = \sigma_e^B / \varepsilon_e^B$ to Equation (6), we get

$$\varepsilon_e = \varepsilon_e^M \left(1 + \frac{\frac{\varepsilon_e^B}{\varepsilon_e^M} - 1}{\frac{\sigma_e^M / \varepsilon_e^M}{\sigma_e^B / \varepsilon_e^B} + 1} \right). \quad (7)$$

Given $\alpha = \varepsilon_e^B / \varepsilon_e^M$ and $\beta = \sigma_e^B / \sigma_e^M$, Equation (7) can be simplified as

$$\varepsilon_e = \varepsilon_e^M \left(1 + \frac{\alpha\beta - \beta}{\alpha + \beta} \right). \quad (8)$$

Here we define α as the ratio of elastic strain limit between the B2 phase and the MG matrix that reflects the relative elastic recovery capability of the B2 phase, and β represents the ratio of strength between the B2 phase and the MG matrix, reflecting the strengthening effect. According to Equation (8), we can get the elastic strain limit of plastically predeformed B2-BMGC related to the factors α and β , as shown in Fig. 4c. For a given β , the elastic strain limit of the plastically predeformed B2-BMGC will monotonically increase with α , which implies that increasing the elastic recovery capability of the B2 phase will increase the elastic strain limit of the B2-BMGC. For example, when $\beta=0.50$, the elastic strain limit of the plastically predeformed B2-BMGC can increase from 2.0% to 2.7%, with α increasing from 1 to 4. When $\beta=0.75$, the elastic strain limit of the plastically predeformed B2-BMGC can increase from 2.0% to 2.9%, with α ranging from 1 to 4. When $\beta=1.00$, the elastic strain limit of the plastically predeformed B2-BMGC can increase from 2.0% to 3.2%. Obviously, large values of α and β can remarkably increase the elastic strain limit of the B2-BMGC. Therefore, Eq. 8 and Fig. 4c demonstrates that the elastic strain limit of a plastically predeformed B2-BMGC can be well tailored by tuning α and β .

With a predeformation of more than 10% total strain (elastic and plastic deformation), the B2 phase underwent a large plastic deformation and was strain-hardened to high strength, as schematically shown in Fig. 4a. Meanwhile, the MG matrix was also plastically deformed and its strength invariable⁴⁰. When unloading, the B19' phase gradually reversely transformed to the B2 phase (see XRD patterns in Fig. 3a). Due to B19'→B2 reverse transformation, the B2 phase recovered to a large quasi-elastic strain ε_{AD} of more than 6%⁴¹, which is much larger than the 2% of the MG. Clearly, in the plastically predeformed B2-BMGC, there is an elastic strain recovery mismatch, so both could not elastically recover freely. At the beginning of elastic recovery, both the B2 phase and the MG matrix could elastically recover to ε_B , where the MG matrix elastically recovered to a zero stress status while the B2 phase was still at a tensile stress of σ_E . Then, the B2 phase further recovered forwards the zero stress but the MG matrix would inhibit this elastic recovery, leaving the MG matrix to be squeezed into a compressive stress state. Therefore, the plastically predeformed B2-BMGC stayed in a complicated microscopical internal stress state: the B2 phase stayed in a tensile stress (σ_E) with a corresponding elastic tensile strain (ε_{DC}), and the MG matrix stayed in a compressive stress (σ_F) with a corresponding elastic compressive strain (ε_{BC}), as shown in Fig. 4a, 4b, and 4d-III. The finite element modeling (FEM) result in Fig. 4e shows that the stress state in the plastically predeformed B2-BMGC is truly compressive in the MG matrix but tensile in the B2 phase, which is basically consistent with the above analysis in Fig. 4a, 4b, and 4d, as well as the stress concentration near the interface.

When reloaded, the compressed MG matrix firstly elastically recovered to the zero stress state from the originally compressive stress state. Further loading caused the MG matrix to be in a tensile stress state. Meanwhile, the former B2 phase recovering from B19' in the plastically predeformed B2-BMGC would transform to B19' again. Theoretically, the apparent elastic strain limit of the plastically predeformed B2-BMGC is $|\varepsilon_{BC}| + \varepsilon_{BA} = |0 \sim -2\%| + 2\% = 0 \sim 4\%$ ($\varepsilon_{BC} = 2\%$ is an ideal value that can not be reached unless the B2 phase possesses a high enough strength and superelasticity), as shown in Fig. 4a. Obviously, a large elastic strain limit of about 2.7% for the plastically predeformed B2-BMGC is reasonable.

Figure 5 shows the tensile yield strength-elastic strain limit data from previous reported Cu-, Zr-, and Ti-based BMGCs and the present B2-BMGC. The line $\varepsilon = 2.0\%$ is a typical elastic strain limit for monolithic BMGs. For the previous reported BMGCs^{15-19,22,42,43}, they are located on the left of the line $\varepsilon = 2.0\%$. Their elastic strain limit approximately ranges from 1.4% ~ 1.9%, with yield strength ranging from 900 MPa to 1560 MPa. As to the plastically predeformed B2-BMGC, they are shown on the upper right corner of the diagram, and are obviously away from the line $\varepsilon = 2.0\%$, exhibiting a good combination of large elastic strain limit and high strength, as shown in Fig. 5a.

In summary, this study demonstrates that the metastable B2 phase can effectively promote multiple shear bands and thus significantly improve the plastic deformation capability of B2-BMGCs, and plastically predeformed B2-BMGCs can exhibit a large elastic strain limit. These unique mechanical properties are attributed to the reversible B2↔B19' phase transformation and the complicated stress states of the MG matrix and the second phase. This finding implies that the elastic properties of BMGCs can be tailored by carefully choosing the reinforcer, with suitable treatment, and can be potentially used as elastic devices or special elastic structure components in engineering fields.

Methods

MGC alloy production. The B2-BMGCs with nominal chemical compositions of $Zr_{48}Cu_{47.5}Al_4Nb_{0.5}$ were prepared by arc melting the elements with purity better than 99.9%, and by casting into a copper mold. Ingots of diameter 3 mm and length 85 mm were produced.

Microstructure characterization. The phases of the BMGC ingots were characterized by X-ray diffraction (XRD) using a Rigaku diffractometer (SmartLab) with Cu K α radiation and an in-situ loading unit. The structure of the B2/MG interface was observed under a JEM-2100F high-resolution transmission electron microscope (HRTEM). The microstructure was also examined by using a JEM 6490

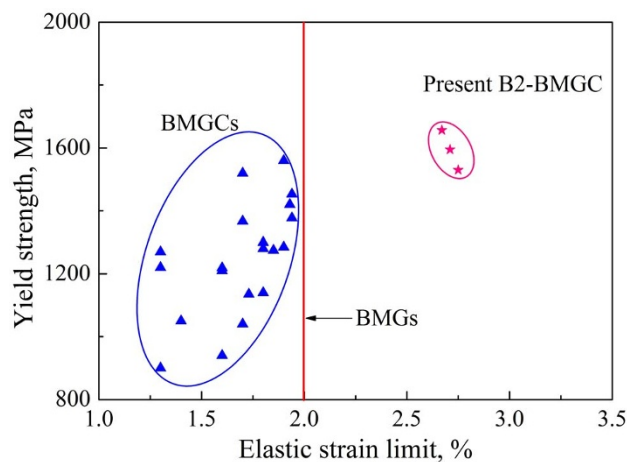


Figure 5 | Plot of tensile yield strength-elastic strain limit for previous reported BMGCs^{15-19,22,42,43} and the present B2-BMGCs subjected to tensile deformation. It shows that the plastically predeformed B2-BMGC possesses a large elastic strain limit and a relatively high strength.



scanning electronic microscope (SEM) and a Carl Zeiss optical microscope (OM). The volume fraction was determined from the OM images.

Tensile test. The tensile samples are in a dog-bone shape. Its gauge length is 10 mm and the dimension of the cross-section is $1 \times 1 \text{ mm}^2$. The tensile samples were prepared by the electric spark method. The lateral surfaces of all tensile samples were ground and finely polished using a 1.0 μm diamond paste. Tensile tests were conducted in an Instron testing machine at room temperature, using a constant strain rate of $1 \times 10^{-4} \text{ s}^{-1}$. In determining the tensile properties of the composite, five tensile samples were tested. Their average values and standard deviations were calculated. The deformed samples were investigated by SEM to reveal the deformation and fracture features.

Finite element modeling. Finite element modeling was utilized to undertake stress analysis for the plastic predeformation of the B2-BMGC. The constitutive equations were directly acquired from the true stress-strain curves of the B2 and MG matrix. The shear stress, von Mises stress and elastic strain of the B2 and MG matrix were measured and compared.

- Mayers, M. A. & Chawla, K. K. *Mechanical behavior of materials* [71–160] (Prentice Hall, New Jersey, 1999).
- Jang, D. & Greer, J. R. transition from a strong-yet-brittle to stronger-yet-ductile state by size reduction of metallic glass. *Nature Mater.* **9**, 215 (2010).
- Tian, L. *et al.* Approaching the ideal elastic limit of metallic glasses. *Nature Commun.* **3**, 609 (2012).
- Deng, Q. S. *et al.* Uniform tensile elongation in framed submicron metallic glass specimens in the limit of suppressed shear banding. *Acta Mater.* **59**, 6511 (2011).
- Jiang, Q. K. *et al.* Super elastic strain limit in metallic glass films. *Sci. Rep.* **2**, 852 (2012).
- Zhang, Z. F., Eckert, J. & Schultz, L. Difference in compressive and tensile fracture mechanisms of $\text{Zr}_{50}\text{Cu}_{20}\text{Al}_{10}\text{Ni}_8\text{Ti}_3$ bulk metallic glass. *Acta Mater.* **51**, 1167 (2003).
- Zhang, Z. F., Wu, F. F., He, G. & Eckert, J. Mechanical properties, damage and fracture mechanisms of bulk metallic glass materials. *J. Mater. Sci. Technol.* **23**, 747 (2007).
- Wu, F. F., Zhang, Z. F. & Mao, S. X. Size-dependent shear fracture and global tensile plasticity of metallic glasses. *Acta Mater.* **57**, 257 (2009).
- Wu, F. F. *et al.* Shear stability of metallic glasses. *Int. J. Plast.* **27**, 560 (2011).
- Kato, H. *et al.* High strength and good ductility of $\text{Zr}_{55}\text{Al}_{10}\text{Ni}_5\text{Cu}_{30}$ bulk glass containing ZrC particles. *Scripta Mater.* **43**, 503 (2000).
- Inoue, A. *et al.* Unusual room-temperature compressive plasticity in nanocrystal-toughened bulk copper-zirconium glass. *Philos. Mag. Lett.* **85**, 221 (2005).
- Fan, C., Louzguine, D. V., Li, C. F. & Inoue, A. Nanocrystalline composites with high strength obtained in Zr-Ti-Ni-Cu-Al bulk amorphous alloys. *Appl. Phys. Lett.* **75**, 340 (1999).
- Louzguine, D. V., Kato, H. & Inoue, A. High-strength Cu-based crystal-glassy composite with enhanced ductility. *Appl. Phys. Lett.* **84**, 1088 (2004).
- Hays, C. C., Kim, C. P. & Johnson, W. L. Microstructure controlled shear band pattern formation and enhanced plasticity of bulk metallic glasses containing in situ formed ductile phase dendrite dispersions. *Phys. Rev. Lett.* **84**, 2901 (2000).
- Hofmann, D. C. *et al.* Designing metallic glass matrix composites with high toughness and tensile ductility. *Nature* **451**, 1085 (2008).
- Hofmann, D. C. *et al.* Development of tough, low-density titanium-based bulk metallic glass matrix composites with tensile ductility. *PNAS* **105**, 20136 (2008).
- Qiao, J. W. *et al.* Tensile deformation micromechanisms for bulk metallic glass matrix composites: From work-hardening to softening. *Acta Mater.* **59**, 4126 (2011).
- Qiao, J. W. In-situ dendrite/Metallic glass matrix composites: a review. *J. Mater. Sci. Technol.* **29**, 685 (2013).
- Szuecs, F., Kim, C. P. & Johnson, W. L. Mechanical properties of $\text{Zr}_{56.2}\text{Ti}_{13.8}\text{Nb}_{5.0}\text{Cu}_{6.9}\text{Ni}_{5.6}\text{Be}_{12.5}$ ductile phase reinforced bulk metallic glass composite. *Acta Mater.* **49**, 1507 (2001).
- Otsuka, K. & Ren, X. Physical metallurgy of Ti-Ni-based shape memory alloys. *Prog. Mater. Sci.* **50**, 511 (2005).
- Oh, Y. S., Kim, C. P., Lee, S. & Kim, N. J. Microstructure and tensile properties of high-strength high-ductility Ti-based amorphous matrix composites containing ductile dendrites. *Acta Mater.* **59**, 7277 (2011).
- Kim, C. P., Oh, Y. S., Lee, S. & Kim, N. J. Realization of high tensile ductility in a bulk metallic glass composite by the utilization of deformation-induced martensitic transformation. *Scripta Mater.* **65**, 304 (2011).
- Wu, Y. *et al.* Ductilizing bulk metallic glass composite by tailoring stacking fault energy. *Phys. Rev. Lett.* **109**, 245506 (2012).

- Wu, Y. *et al.* Bulk metallic glass composites with transformation-mediated work-hardening and ductility. *Adv. Mater.* **22**, 2770 (2010).
- Song, K. K. *et al.* Triple yielding and deformation mechanisms in metastable $\text{Cu}_{47.5}\text{Zr}_{47.5}\text{Al}_5$ composites. *Acta Mater.* **60**, 6000 (2012).
- Pauly, S. *et al.* Microstructural heterogeneities governing the deformation of $\text{Cu}_{47.5}\text{Zr}_{47.5}\text{Al}_5$ bulk metallic glass composites. *Acta Mater.* **57**, 5445 (2009).
- Liu, Z. Q. *et al.* Microstructural tailoring and improvement of mechanical properties in CuZr-based bulk metallic glass composites. *Acta Mater.* **60**, 3128 (2012).
- Wu, F. F. *et al.* Plastic stability of metallic glass composites under tension. *Appl. Phys. Lett.* **103**, 151910 (2013).
- Wu, F. F., Chan, K. C., Li, S. T. & Wang, G. Stabilized shear banding of ZrCu-based metallic glass composites under tensile loading. *J. Mater. Sci.* **49**, 2164 (2014).
- Pauly, S. *et al.* Transformation-mediated ductility in CuZr-based bulk metallic glasses. *Nature Mater.* **9**, 473 (2010).
- Louzguine-Luzgin, D. V. *et al.* Deformation and fracture behavior of metallic glassy alloys and glassy-crystal composites. *Metall. Mater. Trans. A* **42A**, 1504 (2011).
- Louzguine, D. V. *et al.* High-strength and ductile glassy-crystal Ni-Cu-Zr-Ti composite exhibiting stress-induced martensitic transformation. *Philos. Mag. A* **89**, 2887 (2009).
- Seo, J. W. & Schryvers, D. TEM investigation of the microstructure and defects of CuZr martensite. Part I: Morphology and twin systems. *Acta Mater.* **46**, 1165 (1998).
- Seo, J. W. & Schryvers, D. TEM investigation of the microstructure and defects of CuZr martensite. Part II: Planar defects. *Acta Mater.* **46**, 1177 (1998).
- Song, K. K. *et al.* Correlation between the microstructures and the deformation mechanisms of CuZr-based bulk metallic glass composites. *AIP Advances* **3**, 012116 (2013).
- Wu, F. F. *et al.* Strength asymmetry of ductile dendrites reinforced Zr- and Ti-based composites. *J. Mater. Res.* **21**, 2331 (2006).
- Wu, F. F. *et al.* Effect of annealing temperature on a Ti-based metallic glass composite lamella confined by commercially pure titanium. *Philos. Mag. Lett.* **94**, 233 (2014).
- Inoue, A. Stabilization of metallic supercooled liquid and bulk amorphous alloys. *Acta Mater.* **48**, 279 (2000).
- Ashby, M. F. & Greer, A. L. Metallic glasses as structural materials. *Scripta Mater.* **54**, 321 (2006).
- Han, Z., Yang, H., Wu, W. F. & Li, Y. Invariant critical stress for shear banding in a bulk metallic glass. *Appl. Phys. Lett.* **93**, 231912 (2008).
- Hao, S. *et al.* A transforming metal nanocomposite with large elastic strain, low modulus, and high strength. *Science* **339**, 1191 (2013).
- Wu, F. F. *et al.* Effect of annealing temperature on the mechanical properties and fracture mechanisms of a $\text{Zr}_{56.2}\text{Ti}_{13.8}\text{Nb}_{5.0}\text{Cu}_{6.9}\text{Ni}_{5.6}\text{Be}_{12.5}$ bulk metallic glass composite. *Phys. Rev. B* **75**, 134201 (2007).
- Jeon, C. *et al.* High tensile ductility of Ti-based amorphous matrix composites modified from conventional Ti-6Al-4V titanium alloy. *Acta Mater.* **61**, 3012 (2013).

Acknowledgments

This work was supported by the Research Grants Council of the Hong Kong Special Administrative Region, China (Project No. PolyU 511211), and the National Natural Science Foundation of China (NSFC) under Grant Nos. 50901038, and 50931005.

Author contributions

F.W. and K.C. designed the study. F.W., S.J., and S.C. conducted the experiments. F.W., K.C., and G.W. analysed the results and wrote the manuscript.

Additional information

Competing financial interests: The authors declare no competing financial interests.

How to cite this article: Wu, F.F., Chan, K.C., Jiang, S.S., Chen, S.H. & Wang, G. Bulk metallic glass composite with good tensile ductility, high strength and large elastic strain limit. *Sci. Rep.* **4**, 5302; DOI:10.1038/srep05302 (2014).



This work is licensed under a Creative Commons Attribution 4.0 International License. The images or other third party material in this article are included in the article's Creative Commons license, unless indicated otherwise in the credit line; if the material is not included under the Creative Commons license, users will need to obtain permission from the license holder in order to reproduce the material. To view a copy of this license, visit <http://creativecommons.org/licenses/by/4.0/>